oxouranium(VI)[34] (U–O = 2.34 (1), 2.31 (1) Å and N–O = 1.35 (2), 1.36 (2) Å), and aquabis(1,2-dioxopyridinato)dioxouranium hydrate[34] (U–O = 2.35 (1) Å and N–O = 1.38 (2) Å). Notice also that the U–O(*N*-oxide) distances in **3** and **4** are significantly shorter than the U–O(P) distances. This is qualitatively consistent with the *N*-oxide acting as the stronger base site.

The chelate rings in **8–10** are approximately shaped in a chair cyclohexane ring conformation with the U—O=C bond angle greater than the U—O=P bond angle: **8**, 137.6 (5) and 132.6 (3)°; **9**, 140.7 (7) and 136.2 (6)°; **10**, 141.0 (5) and 135.3 (3)°. The ligand "bite" angles (C)O–U–O(P) and nonbonded "bite" distances are 70.4 (2), 70.6 (3), and 71.8 (2)° and 2.781, 2.760, and 2.803 Å, respectively. In **3** and **4**, on the other hand, the chelate rings have a more irregular "twist-chair" cyclohexane configuration with the U—O=P bond angle slightly larger than the U–O–N bond angle: **3**, 129.8 (6) and 127.2 (8)°; **4**, 129.6 (9) and 124.0 (8)°. The bite angles (N)O–U–O(P) and nonbonded bite distances N(O)···(O)P are 70.0 (3)° and 2.742 Å for **3** and 68.3 (4)° and 2.716 Å for **4**. The bite size represents ca. the O···O van der Waals distance in these ligands, a feature that may dictate the dihederal angle between the pyridyl ring and the plane defined by e.g. O(10), P, and C(5) in **3** of approximately 52°. Clearly rotation about the P–C(pyridyl) bond to achieve planarity of the O–P–C–N–O moiety would bring these two oxygen atoms much closer together. In addition, in both structures both the phosphorus and nitrogen atoms of the ligand lie to the same side of the equatorial plane of the uranyl moiety, (0.9 and 0.2 Å, respectively). Obvious differences in packing in the two structures would weaken arguments for this feature based on molecular packing. These structural features in the chelate rings and mode of attachment to the uranyl ion clearly distinguish the (carbamoylmethyl)phosphoryls from the phosphoryl pyridine *N*-oxides in their respective uranyl complexes, and it is of interest to determine if similar differences appear in the structures of lanthanide complexes. It remains to be determined if this structural feature will correlate with differences in extraction abilities for the respective families of ligands.

Acknowledgment. R.T.P. wishes to recognize financial support for this research from the Department of Energy, Office of Basic Energy Sciences (Contract 82ER-40079), and Los Alamos National Laboratory (Contract SP-8614).

Supplementary Material Available: Tables SI and SII listing thermal parameters, Table SIII listing phenyl ring distances and angles, and Figures SI and SII showing chelate ring core structures (7 pages); Tables SIV and SV listing calculated and observed structure factors (19 pages). Ordering information is given on any current masthead page.

(34) Castellato, U.; Vigato, P. A.; Tamburini, S.; Gaziani, R.; Vidali, M. *Inorg. Chim. Acta* **1983**, *72*, 141.

Contribution from Standard Oil Research & Development, Cleveland, Ohio 44128-2837

Interlayer Coordination Environments of Iron, Cobalt, and Nickel in Vanadyl Phosphate Dihydrate, $VOPO_4 \cdot 2H_2O$, Intercalation Compounds

Mark R. Antonio,* Rachael L. Barbour, and Patricia R. Blum

Received August 7, 1986

The results of both structural and spectroscopic studies carried out upon vanadyl phosphate dihydrate ($VOPO_4 \cdot 2H_2O$) intercalation compounds containing iron, cobalt, and nickel are reported. The approximate stoichiometries of these layered compounds are $Fe_{2/5}VOPO_4 \cdot 3H_2O$ (**1**), $Co_{1/5}VOPO_4 \cdot 2H_2O$ (**2**), and $Ni_{1/5}VOPO_4 \cdot 2H_2O$ (**3**). By the use of EXAFS (extended X-ray absorption fine structure), the structures in the immediate vicinity of the transition-metal ion intercalants (Fe, Co, Ni) in **1–3** were determined. The EXAFS results indicate that Fe^{3+} ions in **1** and Co^{2+} ions in **2** have four oxygen nearest neighbors at 1.95 (2) and 2.03 (1) Å, respectively, whereas Ni^{2+} ions in **3** have six oxygen nearest neighbors at 2.05 (2) Å. In addition, there is a second, distant shell of approximately eight oxygen atoms around the Ni^{2+} ions in **3** at 3.02 (4) Å. Powder X-ray diffraction (XRD) measurements show that the V–P–O interlayer distance contracts upon intercalation; that for the pristine $VOPO_4 \cdot 2H_2O$ parent compound is 7.40 (2) Å, whereas those for **1–3** are 6.64, 6.67, and 6.84 (±0.02) Å. A comparison of the infrared (IR), Raman, and XRD data for **1–3** and the parent compound reveals a decrease in short-range order as well as crystallinity upon intercalation. The iron intercalate (**1**) exhibits the greatest structural modification and lattice disorder. In the IR and Raman spectra for **1–3** and $VOPO_4 \cdot 2H_2O$, $[V—O]^{2+,3+}$, $[V=O]^{2+,3+}$, and P—O vibrations all occur between ca. 800 and 1250 cm^{-1}. Raman band frequency shifts that occur upon intercalation by iron, cobalt, and nickel are correlated with the reduction of vanadium in the parent lattice. The thermal analyses of these intercalates, as well as an examination of the infrared OH stretching (3300–3600 cm^{-1}) and bending (1620 cm^{-1}) modes, show differences in the hydration among **1–3**. On the basis of the available structural (EXAFS, XRD) and spectroscopic (IR, Raman) data for **1–3**, we address the interlayer site occupancies of the transition-metal ion intercalants with reference to the structure of the parent V–P–O lattice.

Introduction

Compounds with layered structures have attracted considerable attention,[1] especially for their potential practical applications as solid ionic conductors (electrolytes), anisotropic electronic conductors, inorganic ion exchangers, cathode materials, and catalysts. In particular, experimental and theoretical activity has focused upon the physical properties of intercalation compounds of lamellar inorganic solids.[2–4] The most extensively studied intercalation compounds of quasi-two-dimensional, layered materials include those obtained from iron oxychloride[5–8] (FeOCl), transition-metal

(1) (a) *Crystallography and Crystal Chemistry of Materials with a Layered Structure*; Levy, F. A., Ed.; D. Reidel: Boston, 1975. (b) *Structural Chemistry of Layer-Type Phases*; Hulliger, F., Levy, F. A., Eds.; D. Reidel: Boston, 1976. (c) *Preparation and Crystal Growth of Materials with Layered Structures*; Lieth, R. M. A., Ed.; D. Reidel: Boston, 1977. (d) *Electrons and Phonons in Layered Crystal Structures*; Wieting, T. J., Schluter, M., Eds.; D. Reidel: Boston, 1979.

(2) Van Bruggen, C. F.; Haas, C.; Myron, H. W. *Physica B+C (Amsterdam)* **1980**, *99B+C*, 1–555.

(3) *Intercalated Layered Materials*; Levy, F. A., Ed.; D. Reidel: Boston, 1981.

(4) *Intercalation Chemistry*; Whittingham, M. S., Jacobson, A. J. Eds.; Academic: New York, 1982.

(5) (a) Antonio, M. R.; Averill, B. A. *J. Chem. Soc., Chem. Commun.* **1981**, 382. (b) Averill, B. A.; Kauzlarich, S. M.; Antonio, M. R. *J. Phys. Colloq.* **1983**, *44*(C3), 1373. (c) Averill, B. A.; Kauzlarich, S. M. *Mol. Cryst. Liq. Cryst.* **1984**, *107*, 55.

0020-1669/87/1326-1235$01.50/0

dichalcogenides[9-14] (MY_2), divalent metal phosphorus trisulfides[15,16] (MPS_3), and transition-metal phosphate hydrates [$VOPO_4 \cdot nH_2O$[17-19] and $Zr(HPO_4)_2 \cdot nH_2O$;[20-23] $n = 1, 2$]. For the majority of intercalation compounds prepared to date, complete structural determinations by single-crystal X-ray (or neutron) diffraction methods are unavailable; traditionally, powder X-ray diffraction is the principal method used to infer the orientation and steric relationships between the guest molecule or ion (intercalant) and the host lattice. Recently, however, extended X-ray absorption fine structure (EXAFS) has proven to be a valuable structural technique for investigating the short-range coordination environments of layered materials[24,25] and intercalation compounds.[26-31]

We report herein the results of an EXAFS study of $VOPO_4 \cdot 2H_2O$ intercalation compounds containing iron, cobalt, and nickel, with approximate stoichiometries $Fe_{2/5}VOPO_4 \cdot 3H_2O$ (**1**), $Co_{1/5}VOPO_4 \cdot 2H_2O$ (**2**), and $Ni_{1/5}VOPO_4 \cdot 2H_2O$ (**3**). Using EXAFS, we were able to determine the structure (i.e., number of neighboring atoms and interatomic distances) in the immediate vicinity of the transition-metal ion intercalants. The structural information thus obtained was used to define the sites occupied by the transition-metal intercalants and to explain the observed metal ion loading for **1**–**3**. In addition, the structural and electronic perturbations of the parent $VOPO_4 \cdot 2H_2O$ lattice, due to the presence of the Fe, Co, and Ni intercalants, were examined by infrared (IR) and Raman spectroscopies as well as by powder X-ray diffraction (XRD). Thermal gravimetric analysis (TGA) and differential scanning calorimetry (DSC) were also used to determine the extent of hydration of the parent host and the iron (**1**), cobalt (**2**), and nickel (**3**) intercalation compounds.

Experimental Section

Materials and Methods. The layered vanadyl phosphate dihydrate, $VOPO_4 \cdot 2H_2O$, was prepared as described elsewhere.[17] The X-ray diffraction powder pattern for our $VOPO_4 \cdot 2H_2O$ parent compound is in good agreement with that reported by Ladwig.[17] The parent compound was greenish yellow in color. The $M_xVOPO_4 \cdot yH_2O$ (M = Fe, Co, Ni) intercalation compounds were prepared by the iodide method described by Johnson and Jacobson.[18a-c] After intercalation, all three complexes were a green color, indicating that vanadium reduction had occurred. The iron intercalation compound was the lightest and the nickel compound the darkest green color.

All reagents were used without further purification. Elemental analyses (V, Fe, Co, Ni, P) were performed by inductively coupled plasma-emission spectroscopy (ICP-ES). The water content of the compounds was determined by TGA (thermal gravimetric analysis). Anal. Calcd for $VPO_5 \cdot 2H_2O$ (M_r 197.94): V, 25.7; P, 15.6; H_2O, 18.2. Found: V, 27; P, 16; H_2O, 17.5. Anal. Calcd for **1**, $Fe_{2/5}VPO_5 \cdot 3H_2O$ (M_r 238.29): Fe, 9.4; V, 21.4; P, 13.0; H_2O, 20.1. Found: Fe, 9.7; V, 20; P, 15; H_2O, 21.0. Anal. Calcd for **2**, $Co_{1/5}VPO_5 \cdot 2H_2O$ (M_r 209.73): Co, 5.6; V, 24.3; P, 14.8; H_2O, 17.2. Found: Co, 5.0; V, 24; P, 14; H_2O, 19.2. Anal. Calcd for **3**, $Ni_{1/5}VPO_5 \cdot 2H_2O$ (M_r 209.68): Ni, 5.6; V, 24.3; P, 14.8; H_2O, 17.2. Found: Ni, 6.6; V, 23; P, 14; H_2O, 16.8.

Thermal Titrations. An attempt was made to determine the quantity of vanadium(5+) present in the intercalates **1**–**3** via a thermal-redox titrimetry technique. A weighed portion of each of the intercalation compounds was titrated with a standardized solution of ferrous ammonium sulfate. The ferrous ion reduced the vanadium(5+) to vanadium(4+) in an exothermic reaction. The titration was carried out in an adiabatic cell, and the temperature rise was used to determine the end point of the reaction. The results obtained with the cobalt-containing intercalate (**2**) were completely consistent with the Co(2+) stoichiometry; that is, 60% of the vanadium was found to be pentavalent. The titrimetry data, along with elemental analysis and TGA, yield the following empirical formula for **2**: $[V^{4+}]_{0.4}[V^{5+}]_{0.6}Co_{0.2}P_1O_5 \cdot 2H_2O$. With the iron (**1**) and nickel (**3**) intercalates, however, the thermal titrimetry technique could not be used to reliably determine the V(5+) content. This was due to, in part, interferences from the intercalating cations, Fe^{3+} in **1** and Ni^{2+} in **3**, and secondary redox reactions.

Physical Measurements. All measurements were taken under ambient conditions. Infrared spectra were obtained on Nicolet 7199 (mid-IR) and Nicolet 200 SX (far-IR) Fourier transform infrared (FT-IR) spectrometers. Spectra were recorded at approximately 8-cm^{-1} resolution. For the mid-IR measurements (4000-400 cm^{-1}), the samples were prepared both as KBr pellets and as split (Nujol and Fluorolube) mulls. The mulls were run between KBr windows. For the far-IR measurements (400–100 cm^{-1}), the samples were prepared as Nujol mulls and placed between polyethylene windows.

(6) (a) Eckert, H.; Herber, R. H. *J. Chem. Phys.* **1984**, *80*, 4526. (b) Herber, R. H.; Maeda, Y. *Inorg. Chem.* **1981**, *20*, 1409. (c) Herber, R. H.; Maeda, Y. *Inorg. Chem.* **1980**, *19*, 3411. (d) Herber, R. H.; Rein, A. J. *J. Chem. Phys.* **1980**, *73*, 6345.

(7) (a) Fatseas, G. A.; Palvadeau, P.; Venien, J. P. *J. Solid State Chem.* **1984**, *51*, 17. (b) Rouxel, J.; Palvadeau, P. *Rev. Chim. Miner.* **1982**, *19*, 317. (c) Weiss, A.; Choy, J. H. *Z. Naturforsch., B: Anorg. Chem., Org. Chem.* **1980**, *35B*, 157. (d) Kanamaru, F.; Yamanaka, S.; Koizumi, M.; Nagai, S. *Chem. Lett.* **1974**, 373.

(8) (a) Schaefer-Stahl, H.; Abele, R. *Z. Anorg. Allg. Chem.* **1980**, *465*, 147. (b) Schaefer-Stahl, H.; Abele, R. *Angew. Chem., Int. Ed. Engl.* **1980**, *19*, 477. (c) Schaefer-Stahl, H. *Mater. Res. Bull.* **1980**, *15*, 1091. (d) Schaefer-Stahl, H.; Abele, R. *Mater. Res. Bull.* **1980**, *15*, 1157.

(9) (a) Gamble, F. R.; Osiecki, J. H.; Cais, M.; Pisharody, R.; DiSalvo, F. J.; Geballe, T. H. *Science (Washington, D.C.)* **1971**, *174*, 493. (b) Murphy, D. W.; DiSalvo, F. J.; Hull, G. W., Jr.; Waszczak, J. V. *Inorg. Chem.* **1976**, *15*, 17.

(10) Rao, G. V. S.; Shafer, M. W.; Tsang, J. C. *J. Phys. Chem.* **1975**, *79*, 553.

(11) Beal, A. R.; Liang, W. Y. *Philos. Mag.* **1973**, *27*, 1397.

(12) (a) Weiss, A.; Ruthardt, R. *Z. Naturforsch., B: Anorg. Chem., Org. Chem.* **1973**, *28B*, 522. (b) Schoellhorn, R.; Weiss, A. *Z. Naturforsch., B: Anorg. Chem., Org. Chem.* **1973**, *28B*, 172.

(13) (a) Whittingham, M. S. *Prog. Solid State Chem.* **1978**, *12*, 41. (b) Clement, R. P.; Davies, W. B.; Ford, K. A.; Green, M. L. H.; Jacobson, A. J. *Inorg. Chem.* **1978**, *17*, 2754.

(14) Dines, M.; Levy, R. *J. Phys. Chem.* **1975**, *79*, 1979. (b) Dines, M. B. *J. Chem. Soc., Chem. Commun.* **1975**, *220*. (c) Dines, M. B. *Science (Washington, D.C.)* **1975**, *188*, 1210. (d) Dines, M. B. *Inorg. Chem.* **1978**, *17*, 762.

(15) (a) Clement, R. *J. Am. Chem. Soc.* **1981**, *103*, 6998. (b) Clement, R.; Girerd, J. J.; Morgenstern-Badarau, I. *Inorg. Chem.* **1980**, *19*, 2852. (c) Clement, R. *J. Chem. Soc., Chem. Commun.* **1980**, 647. (d) Clement, R.; Green, M. L. H. *J. Chem. Soc., Dalton Trans.* **1979**, 1566. (e) Audiere, J. P.; Clement, R.; Mathey, Y.; Mazieres, C. *Physica B+C (Amsterdam)* **1980**, *99B+C*, 133.

(16) (a) Yamanaka, S.; Kobayashi, H.; Tanaka, M. *Chem. Lett.* **1976**, 329. (b) Brec, R.; Schleich, D. M.; Ouvrard, G.; Louisy, A.; Rouxel, J. *Inorg. Chem.* **1979**, *18*, 1814. (c) Foot, P. J. S.; Shaker, N. G. *Mater. Res. Bull.* **1983**, *18*, 1973.

(17) Ladwig, G. *Z. Anorg. Allg. Chem.* **1965**, *338*, 266.

(18) (a) Johnson, J. W.; Jacobson, A. J. European Patent Application No. 0051999, Exxon Research and Engineering Co., 1982. (b) Johnson, J. W.; Jacobson, A. J. *Angew. Chem., Int. Ed. Engl.* **1983**, *22*, 412. (c) Johnson, J. W.; Jacobson, A. J. U.S. Patent 4 376 709, Exxon Research and Engineering Co., 1983. (d) Johnson, J. W.; Jacobson, A. J.; Brody, J. F.; Rich, S. M. *Inorg. Chem.* **1982**, *21*, 3820.

(19) (a) Tachez, M.; Theobald, F.; Bernard, J.; Hewat, A. W. *Rev. Chim. Miner.* **1982**, *19*, 291. (b) Beneke, K.; Lagaly, G. *Inorg. Chem.* **1983**, *22*, 1503. (c) Lara, M. M.; Lopez, A. J.; Real, L. M.; Bruque, S.; Casal, B.; Hitzky, E. R. *Mater. Res. Bull.* **1985**, *20*, 549. (d) Lara, M. M.; Real, L. M.; Lopez, A. J.; Gamez, S. B.; Garcia, A. R. *Mater. Res. Bull.* **1986**, *21*, 13.

(20) (a) Constantino, U. *J. Inorg. Nucl. Chem.* **1981**, *43*, 1895. (b) Costantino, U. *J. Chem. Soc., Dalton Trans* **1979**, 402.

(21) (a) Yamanaka, S.; Matsunaga, M.; Hattori, M. *J. Inorg. Nucl. Chem.* **1981**, *43*, 1343. (b) Yamanaka, S.; Horibe, Y.; Tanaka, M. *J. Inorg. Nucl. Chem.* **1976**, *38*, 323.

(22) (a) Clearfield, A.; Tindwa, R. M. *J. Inorg. Nucl. Chem.* **1979**, *41*, 871. (b) Tindwa, R. M.; Ellis, D. K.; Peng, G. Z.; Clearfield, A. *J. Chem. Soc., Faraday Trans. 1* **1985**, *81*, 545.

(23) (a) Johnson, J. W. *J. Chem. Soc., Chem. Commun.* **1980**, 263. (b) Johnson, J. W., U.K. Patent Application 2039910A, Exxon Research and Engineering Co., 1980.

(24) Heald, S. M.; Stern, E. A. *Phys. Rev. B: Solid State* **1977**, *12*, 5549.

(25) Mathey, Y.; Michalowicz, A.; Toffoli, P.; Vlaic, G. *Inorg. Chem.* **1984**, *23*, 897.

(26) Bourdillon, A. J.; Pettifer, R. F.; Marseglia, E. A. *J. Phys. C* **1979**, *12*, 3889.

(27) (a) Kauzlarich, S. M.; Averill, B. A.; Teo, B. K. *Mol. Cryst. Liq. Cryst.* **1984**, *107*, 65. (b) Kauzlarich, S. M.; Teo, B. K.; Averill, B. A. *Inorg. Chem.* **1986**, *25*, 1209.

(28) (a) Alagna, L.; Tomlinson, A. A. G. *J. Chem. Soc., Faraday Trans. 1* **1982**, *78*, 3009. (b) Alagna, L.; Prosperi, T.; Tomlinson, A. A. G.; Ferragina, C.; LaGinestra, A. *J. Chem. Soc., Faraday Trans. 1* **1983**, *79*, 1039.

(29) Michalowicz, A.; Clement, R. *Inorg. Chem.* **1982**, *21*, 3872. (b) Clement, R.; Michalowicz, A. *Rev. Chim. Miner.* **1984**, *21*, 426.

(30) DeRoy, A.; Besse, J. P.; Bondot, P. *Mater. Res. Bull.* **1985**, *20*, 1091.

(31) (a) Heald, S. M.; Stern, E. A. *Synth. Met.* **1979/1980**, *1*, 249. (b) Caswell, N.; Solin, S. A.; Hayes, T. M.; Hunter, S. J. *Physica B+C (Amsterdam)* **1980**, *99B+C*, 463. (c) Bouat, J.; Bonnin, D.; Facchini, L.; Beguin, F. *Synth. Met.* **1983**, *7*, 233. (d) Feldman, J. L.; Skelton, E. F.; Ehrlich, A. C.; Dominquez, D. D.; Elam, W. T.; Qadri, S. B.; Lytle, F. A. *Solid State Commun.* **1984**, *49*, 1023.

Raman spectra of the neat powdered samples were obtained with a SPEX Ramalog 1401 equipped with a 0.85-m Czerny-Turner double monochromator, an RCA C31034 cooled photomultiplier, and a Spectra-Physics 165 argon-ion laser (5145 Å exciting line). The spectral range was approximately 1200–200 cm^{-1}, and the spectral slit width was ca. 3 cm^{-1}. Spectra were recorded by using ca. 50 mW of power at the sample.

Powder X-ray diffraction data were obtained by using a Scintag X-ray diffractometer and graphite-monochromated Cu Kα radiation. Thermal analyses (TGA and DSC) were performed with a Du Pont 1090 thermal analyzer. The data were recorded from ambient temperature to 600 °C, while the samples were kept under an atmosphere of flowing dinitrogen.

X-ray Absorption Measurements. The X-ray absorption experiments were performed on pressed pellet samples. The pellets were prepared by grinding each of the intercalation and model compounds to a fine powder with boron nitride (Alfa Chemical Co.) and compressing the homogeneous mixtures to a uniform thickness in aluminum sample cells. The compounds $Fe(NO_3)_3 \cdot 9H_2O$, $Co(NO_3)_2 \cdot 6H_2O$, and $Ni(NO_3)_2 \cdot 6H_2O$, used as models for the X-ray absorption measurements, were obtained from Alfa Chemical Co. The measurements were performed at the Cornell High Energy Synchrotron Source (CHESS) on the C-1 EXAFS beam line using the synchrotron radiation from the Cornell Electron Storage Ring (CESR); CESR operated at 5.2 GeV with approximately 10–35 mA of electron beam current.

The iron, cobalt, and nickel K-edge X-ray absorption data were recorded in the transmission mode under ambient conditions. The white synchrotron radiation from the CESR was monochromated by a fixed-offset, separated silicon ⟨111⟩ crystal device. Prior to each scan, the crystal monochromator was detuned to reduce the harmonic-to-fundamental beam intensity ratio. Incident (I_0) and transmitted (I) beam intensities were monitored with flow-type ionization chambers using a combination of dinitrogen (I_0) and argon (I) detecting gases. The X-ray absorption data were recorded with an integration time of 1–2 s/point by constant I_0 accumulation. The photon energy was scanned from about 200 eV below to about 800 eV above the Fe, Co, and Ni K-edges (7112.0, 7708.9, and 8332.8 eV, respectively).[32] Each X-ray absorption spectrum contained approximately 170 points at discrete energy increments in steps of approximately constant k (the photoelectron wave vector) in $Å^{-1}$. The incremental energy steps ranged from 1 eV/point at the K-edge photoabsorption thresholds to 8 eV/point at the end of each scan. All of the data were collected under low-resolution (ca. 5 eV) conditions.

EXAFS Data Analysis. The EXAFS data reduction[33] and curve fitting were performed as described elsewhere.[34] The raw Fe, Co, and Ni K-edge X-ray absorption data, in the form ln (I_0/I) vs. E (in eV), and the corresponding background-subtracted EXAFS data, in the form $k^3\chi(k)$ vs. k (in $Å^{-1}$), for **1–3** are given as supplementary material.

The Fourier-filtered M–O (M = Fe, Co, Ni) EXAFS, $k^3\chi(k)$ vs. k, were modelled with the conventional single-scattering formulation of the EXAFS effect:[35]

$$k^3\chi(k) = \sum_j B_j F_j(k_j) k_j^2 r_j^{-2} \exp[-2r_j/\lambda(k_j)] \exp[-2\sigma_j^2 k_j^2] \sin [2k_j r_j + \phi_j(k_j)] \quad (1)$$

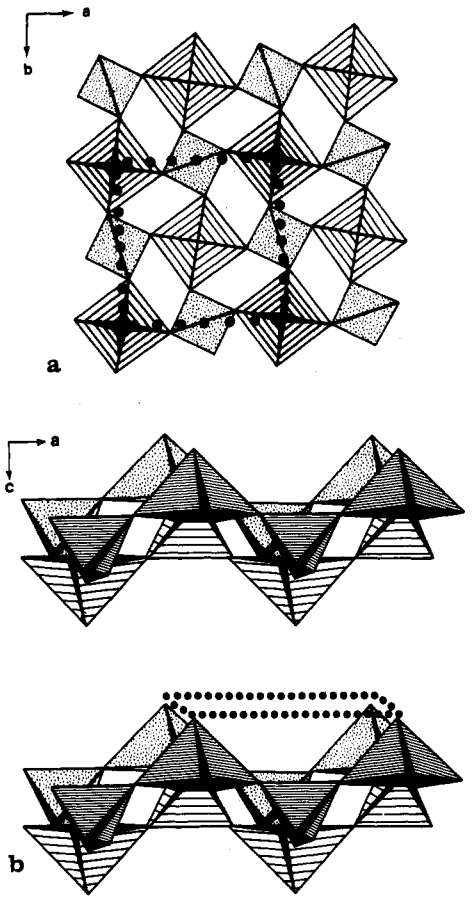

Figure 1. Schematic drawing of the structure of the $VOPO_4 \cdot 2H_2O$ lattice as viewed down (a) the c axis, in which the four thick-lined VO_6 octahedra are located on a plane that is above that containing the four thin-lined VO_6 octahedra and (b) the b axis, in which water molecules have been omitted for clarity (hence, the VO_6 octahedra are represented as square pyramids). The unit cell repeat distance along a and b is 6.202 (2) Å, and that for c is 7.410 (1) Å.[39] Oxygen atoms are located at the corners of the polyhedra. The dotted lines define the perimeter of the pocket.

Theoretical amplitude $F_j(k_j)$ and phase $\phi_j(k_j)$ functions calculated by Teo and Lee[36] were used in the curve fittings. For each k value, $F(k)$ and $\phi(k)$ were interpolated from the theoretical values[37] by using cubic functions. The Fourier-filtered EXAFS for **1–3** were fit with a single-shell model (j = O) of eq 1. Five parameters were varied in the nonlinear least-squares refinements: (i) a scale factor, B; (ii) a Debye–Waller factor, σ; (iii) an interatomic distance, r; (iv) an energy threshold difference, ΔE_0^P; (v) an electron mean-free-path parameter, η. In eq 1, the term $\exp[-2r/\lambda(k)]$ was used to account for the lifetime of the core hole and inelastic scattering losses. The electron mean free path, $\lambda(k)$, was approximated by $\lambda(k) = k^n/\eta$,[38] where n = 1, 2, and 3 were used in the curve fitting. The goodness of the fits obtained for the parameterizations with the electron mean-free-path term (n = 1, 2, 3) were all virtually equivalent; they were, in turn, at least two times better than the goodness of the fits without the electron mean-free-path term (i.e., $\exp[-2r\eta/k^n]$ = 1). The curve-fitting results for the interatomic distance parameters were invariant with respect to the functional form of the mean free path. However, strong correlations between σ, η, and n (for n = 1, 2, 3) were observed in the nonlinear least-squares curve fitting. For all of the parameter refinements reported herein, n was fixed at 3 since the values thus obtained for σ were the most reasonable, based upon the known structural and spectroscopic data for the M–O interactions in the hexaaquametal ion nitrate model compounds.

(32) Bearden, J. A.; Burr, A. F. *Rev. Mod. Phys.* **1967**, *39*, 125.

(33) (a) For conversion to $k(Å^{-1})$ space ($k = [0.263(E - E_0^{expt})]^{1/2}$), the experimental energy thresholds (E_0^{expt}, eV) for the Fe, Co, and Ni K-edge EXAFS data for **1–3** were chosen at 7144, 7735, and 8369 eV, respectively. These E_0^{expt} values are approximately 20 eV above the corresponding edge position energies (E_0^P, the photon energy at half-height of the edge jump) for the Fe, Co, and Ni data for **1–3** (7122.6, 7715.9, and 8349.1 eV). The data were weighted by k^3 and the background was removed by using four sections (ca. 3.2 $Å^{-1}$ each) of cubic spline functions. The EXAFS was normalized by dividing by the edge jumps (0.53, 0.68, and 0.44 for **1–3**, respectively) and also corrected for the fall-off in the absorption cross section according to $\mu_0/\rho = C\lambda^3 - D\lambda^4$,[33b] in which μ_0/ρ is the mass absorption coefficient, λ is the wavelength of the incident X-radiation, and the parameters C and D (associated with the X-ray absorbing atom) are,[33c] respectively, 126 and 27.2 for Fe, 141 and 33.2 for Co, and 158 and 40.1 for Ni. (b) Victoreen, J. A. *J. Appl. Phys.* **1948**, *19*, 855. (c) *International Tables for X-ray Crystallography*; Macgillavry, C. H., Rieck, G. D., Lonsdale, K., Eds.; Kynoch: Birmingham, England, 1968; Vol. III, pp 171–173.

(34) (a) Teo, B.-K.; Antonio, M. R.; Averill, B. A. *J. Am. Chem. Soc.* **1983**, *105*, 3751. (b) Teo, B.-K. *EXAFS: Basic Principles and Data Analysis*; Springer-Verlag: Berlin, 1986. (c) Lee, P. A.; Citrin, P. H.; Eisenberger, P.; Kincaid, B. M. *Rev. Mod. Phys.* **1981**, *53*, 769.

(35) (a) Sayers, D. E.; Lytle, F. W.; Stern, E. A. In *Advances in X-ray Analysis*; Henke, B. L., Newkirk, J. B., Mallett, R. G, Eds.; Plenum: New York, 1970; Vol. 13, pp 248–271. (b) Ashley, C. A.; Doniach, S. *Phys. Rev. B: Solid State* **1975**, *11*, 1279. (c) Lee, P. A.; Pendry, J. B. *Phys. Rev. B: Solid State* **1975**, *11*, 2795.

(36) Teo, B.-K.; Lee, P. A. *J. Am. Chem. Soc.* **1979**, *101*, 2815.

(37) The theoretical values of the EXAFS functions $F(k)$ and $\phi(k)$ were obtained in ref 36 (Table VII) for the central atom phases $\phi_{Fe}{}^a$, $\phi_{Co}{}^a$, and $\phi_{Ni}{}^a$ and in ref 38a (Table II, supplementary material; for β = 180°), for the oxygen backscattering phase $\phi_O{}^b$ and amplitude F_O functions.

(38) (a) Teo, B.-K. *J. Am. Chem. Soc.* **1981**, *103*, 3990. (b) Alberding, N.; Crozier, E. D. *Phys. Rev. B: Condens. Matter* **1983**, *27*, 3374.

The oxygen coordination numbers (N) for **1–3** were determined via the *fine adjustment* method *based* on *models* (FABM)[34a,b] according to $N = B/S$, where the amplitude reduction factors (S) were obtained from the EXAFS analysis of the model compounds. The pertinent B vs. σ and ΔE_0^P vs. Δr FABM correlation curves as well as their associated regression coefficients are given as supplementary material. A detailed description of the FABM method as applied to the EXAFS data for **1–3** is also presented in the supplementary material.

Results and Discussion

Site Availability. The crystal structure of $VOPO_4 \cdot 2H_2O$ has been described by Tietz.[39] Parts a and b of Figure 1 show schematic projections of the structure onto the *ab* and *ac* planes, respectively, of the tetragonal unit cell. The structure consists of layers of PO_4 tetrahedra linked to distorted VO_6 octahedra (with C_4 symmetry) by corner-sharing phosphate oxygen atoms. The two axial oxygen atoms positions in the VO_6 octahedra are interpreted as being due to short $[V{=}O]^{3+}$ (1.567 (5) Å) and long $V{-}OH_2$ (2.233 (6) Å) interactions.[39] From Figure 1, it can be seen that a potential intercalation site is defined by four in-plane vanadyl groups, i.e., there are 6.20 × 6.20 Å pockets, corresponding to the *a* and *b* unit cell repeat distances, within each layer. The perimeter of the pocket (or cavity) is schematically outlined with dotted lines in Figure 1. Each pocket encompasses 2.5 unit cells, and thus, *five vanadium atoms are associated with each pocket.*

The calculated stoichiometries for **1–3** indicate that both the cobalt (**2**) and nickel (**3**) intercalates have an M/V (M = Co, Ni) ratio of apporoximately 1/5, whereas the Fe/V ratio for the iron intercalate (**1**) is ca. 2/5, or double the ratio for **2** and **3**. Given the aforementioned site availability, it is proposed that the intercalant metal ions in **2** and **3** are distributed among nonadjoining pockets within the parent lattice. It is further proposed that the intercalant metal ions in **1** are more densely distributed among the available sites such that there may now be iron atoms in adjoining pockets. To provide support for the postulated site occupancies, we have determined the local structures (e.g., interatomic distances, coordination numbers, and Debye–Waller factors) of the transition-metal ion intercalants in **1–3** by using EXAFS.

EXAFS Data. Fourier transforms of the normalized, background-subtracted Fe, Co, and Ni EXAFS, $k^3\chi(k)$ vs. k, of **1–3** are shown as the solid curves in parts a–c of Figure 2. Each Fourier transform exhibits one principal peak at ca. 1.7 Å (before phase shift correction) that is presumably due to backscattering from neighboring oxygen atoms. In addition, the Fourier transform of the Ni EXAFS data for **3** (Figure 2c) clearly exhibits a second, broad peak at 2.4 Å (uncorrected), which is assigned to Ni–O (and/or Ni–P) backscatterings. The small peaks between 2.0 and 3.0 Å (uncorrected) in the Fourier transforms of the Fe and Co EXAFS data (Figure 2a,b) for **1** and **2**, respectively, may also be due to backscattering from distant neighbors. Unfortunately, the variability in the shapes and positions of these distant peaks upon different background removal treatments precludes a detailed structural analysis with the available data.

The dashed curves shown in Figure 2a–c are the window functions used to Fourier filter and back-transform the M–O (M = Fe, Co, Ni) backscatterng contributions from distance space (Å) to k space ($Å^{-1}$). The resulting Fourier-filtered EXAFS, over the region 3–12 $Å^{-1}$ for **1–3** (Figure 3, solid curves), were employed in the nonlinear least squares curve fitting. The best fits are depicted as dashed curves in Figure 3a-c. The resulting least squares refined structural parameters for 1–3 and the model compounds are listed in Table I. The accuracy of the M–O distances (ca. ±0.03 Å) is judged from the model compounds $Fe(NO_3)_3 \cdot 9H_2O$,[40a] $Co(NO_3)_2 \cdot 6H_2O$,[40b] and $Ni(NO_3)_2 \cdot 6H_2O$,[40c] which were measured and analyzed in the same fashion. In order to determine the coordination numbers and to improve the accuracy of the best-fit interatomic distances, the fine adjustment method based on models[34a,b] (FABM) was applied to the EXAFS data of **1–3**.

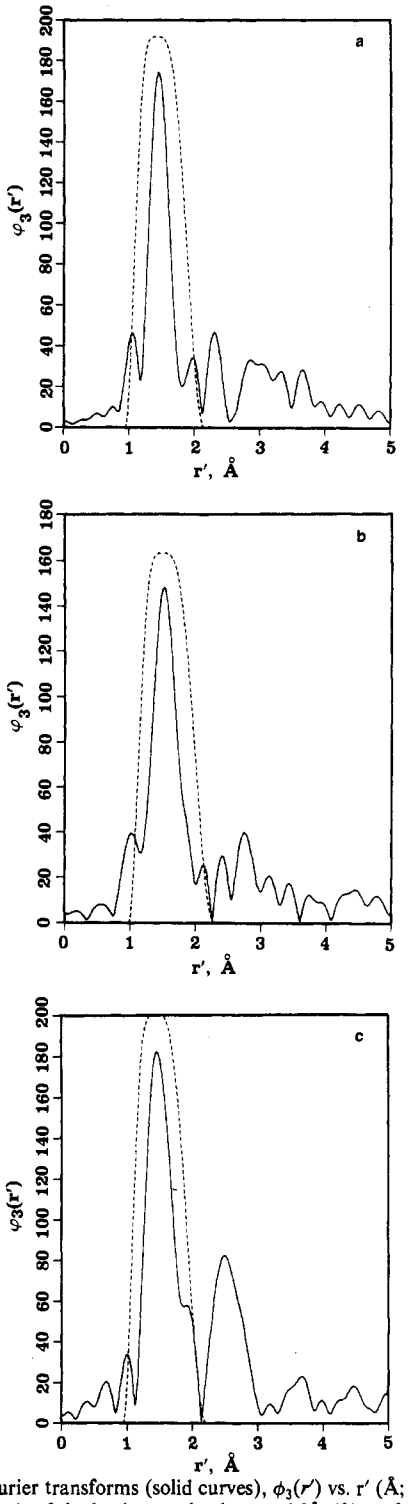

Figure 2. Fourier transforms (solid curves), $\phi_3(r')$ vs. r' (Å; before phase shift correction), of the background-subtracted $k^3\chi(k)$ vs. k transmission EXAFS data and filtering windows (dashed curves): (a) Fe K-edge of $Fe_{2/5}VPO_5 \cdot 3H_2O$ (**1**); (b) Co K-edge of $Co_{1/5}VPO_5 \cdot 2H_2O$ (**2**); (c) Ni K-edge of $Ni_{1/5}VPO_5 \cdot 2H_2O$ (**3**).

The FABM results are also tabulated in Table I. The mean Fe–O interatomic distance [1.95 (2) Å] for **1** is significantly shorter than both the mean Co–O [2.03 (1) Å] and Ni–O [2.05 (2) Å] distances for **2** and **3**, respectively. Each of these distances is consistent with those known for Fe^{3+}–O, Co^{2+}–O, and Ni^{2+}–O interactions, respectively, for a variety of single-crystal X-ray structures.[41] For example, the tetrahedral Fe^{3+}–O_4 and Co^{2+}–O_4

(39) Tietze, H. R. *Aust. J. Chem.* **1981**, *34*, 2035.
(40) (a) Hair, N. J.; Beattie, J. K. *Inorg. Chem.* **1977**, *16*, 245. (b) Prelesnik, B. V.; Gabela, F.; Ribar, B.; Krstanovic, I. *Cryst. Struct. Commun.* **1973**, *2*, 581. (c) Bigoli, F.; Bribanti, A.; Tiripicchio, A.; Camellini, M. T. *Acta Crystallogr., Sect. B: Struct. Crystallogr. Cryst. Chem.* **1971**, *B27*, 1427.

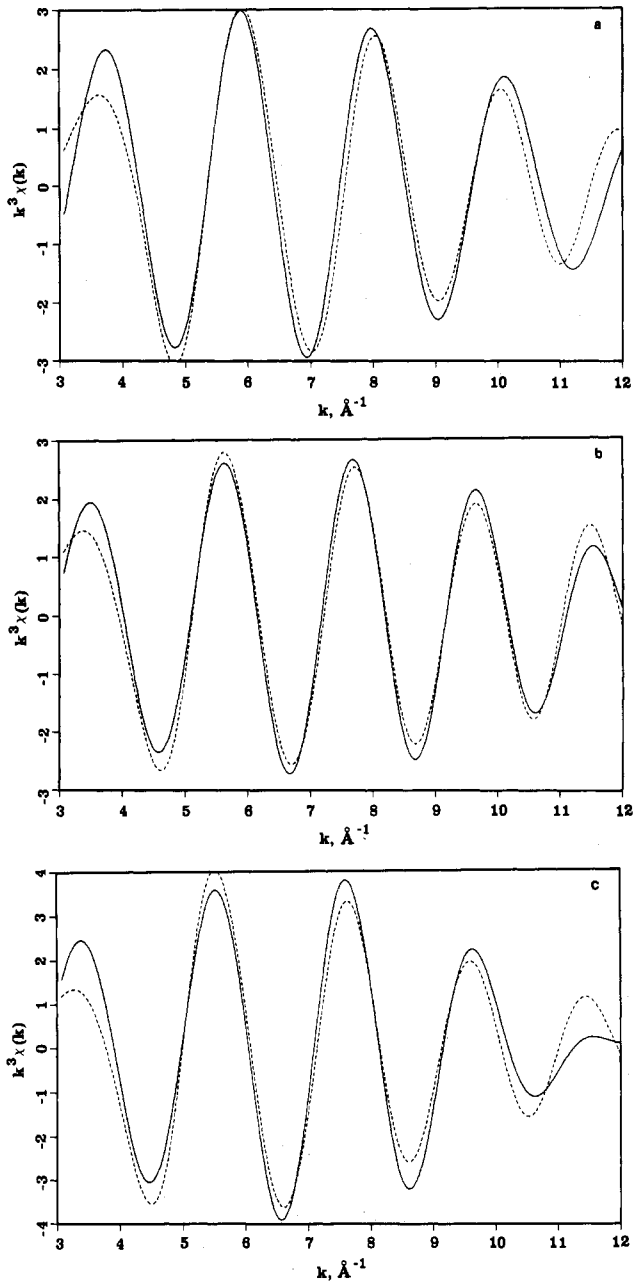

Figure 3. Fourier-filtered $k^3\chi(k)$ vs. k EXAFS (solid curves) and the nonlinear least-squares best fits (dashed curves), based on theoretical functions: (a) Fe K-edge of **1**; (b) Co K-edge of **2**; (c) Ni K-edge of **3**.

groups in $Bi_3(FeO_4)(MoO_4)_2$ and Co_3O_4 have mean Fe–O and Co–O interatomic distances of 1.91 (2)[42a] and 1.99 (2)[42b] Å, respectively. The octahedral Ni^{2+}–O_6 group in hexaaquanickel nitrate has a mean Ni–O interatomic distance of 2.06 (1) Å.[40c] Both Fe and Co have a four-coordinate interlayer oxygen environment in **1** and **2**, respectively, whereas Ni has a six-coordinate interlayer oxygen environment in **3**.

X-ray Diffraction. Compared to the XRD powder pattern data for the parent dihydrate, those for **1–3** (Figure 4) indicate a significant loss of crystallinity upon intercalation (i.e., the number and intensity of observable Bragg reflections decreases dramatically). Of the three intercalation compounds, the powder XRD data for the nickel intercalate (**3**) clearly show the strongest and sharpest Bragg peaks, whereas those data for the iron intercalate (**1**) exhibit the weakest and most diffuse diffraction peaks (Figure 4). The interlayer long-range order is apparently reduced as is evident by the decrease in the intensity of the [001] reflection on going from, in order, the parent material to the Ni (**3**), Co (**2**), and Fe (**1**) intercalation compounds. For **1–3**, intercalation causes the spacing between the vanadyl phosphate layers to contract, thereby reducing the van der Waals gap. The interlayer contraction is presumably due to an electrostatic attraction[18b] between the vanadyl phosphate layers, which bear a net negative charge (because of the partial reduction of the vanadium), and the intercalating cations, which bear a net positive charge. The [001]

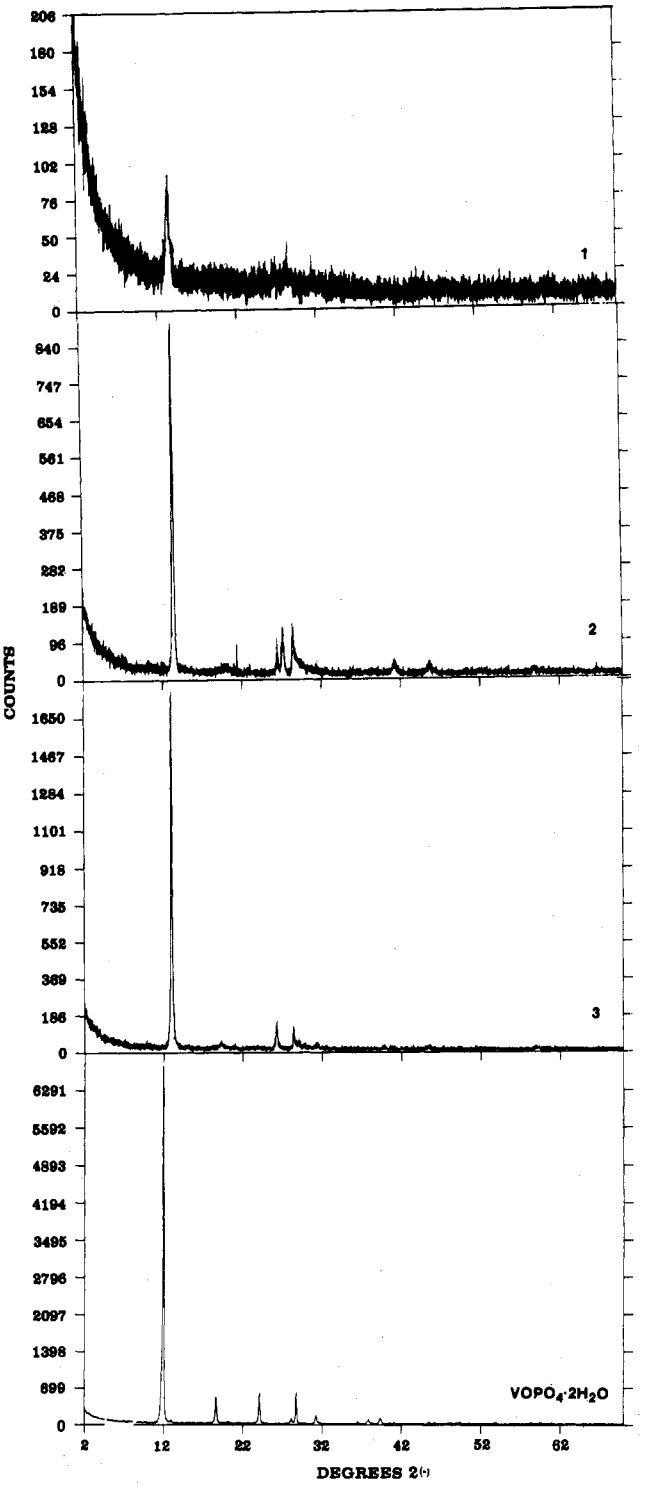

Figure 4. X-ray diffraction powder patterns for **1–3** and the $VOPO_4 \cdot 2H_2O$ parent complex. The intense, low-angle ($12° < 2\theta < 13°$) Bragg peaks are due to [001] reflections (Cu Kα radiation).

(41) (a) Shannon, R. D.; Prewitt, C. T. *Acta Crystallogr., Sect. B: Struct. Crystallogr. Cryst. Chem.* **1969**, *B25*, 925. (b) Brown, I. D.; Shannon, R. D. *Acta Crystallogr., Sect A: Cryst. Phys., Diffr., Theor. Gen. Crystallogr.* **1973**, *A29*, 266.

(42) (a) Jeitschko, W.; Sleight, A. W.; McClellan, W. R.; Weiher, J. F. *Acta Crystallogr., Sect. B: Struct. Crystallogr. Cryst. Chem.* **1976**, *B32*, 1163. (b) Smith, W. L.; Hobson, A. D. *Acta Crystallogr., Sect. B: Struct. Crystallogr. Cryst. Chem.* **1973**, *B29*, 362.

Table I. Best Fit and FABM Interatomic Distances (r), Debye-Waller Factors (σ), and Coordination Numbers (N) with Estimated Standard Deviations (in Parentheses), Energy Threshold Differences (ΔE_0^P), and Scale Factors (B) for the Fe, Co, and Ni K-Edge Transmission EXAFS Data for **1**–**3** and Model Compounds

		dist		amplitude		
compd	term	r, Å	ΔE_0^P,[a] eV	σ, Å	B	N
			Best Fit			
1	Fe–O	1.97 (5)	3.074	0.078 (39)	2.731	*b*
$Fe(NO_3)_3 \cdot 9H_2O$	Fe–O	2.02 (4)	6.702	0.073 (23)	3.877	6
2	Co–O	2.03 (2)	3.230	0.058 (26)	1.772	*b*
$Co(NO_3)_2 \cdot 6H_2O$	Co–O	2.06 (5)	−0.928	0.087 (35)	4.314	6
3	Ni–O	2.02 (4)	−0.599	0.088 (30)	4.482	*b*
$Ni(NO_3)_2 \cdot 6H_2O$	Ni–O	2.04 (2)	2.817	0.076 (20)	3.454	6
			FABM			
1	Fe–O	1.95 (2)	−0.972	0.079 (20)	2.813	3.9 (11)
2	Co–O	2.03 (1)	2.498	0.090 (35)	2.737	3.6 (10)
3	Ni–O	2.05 (2)	6.383	0.076 (20)	3.655	6.3 (10)

[a] These standardized energy threshold differences were obtained according to $\Delta E_0^P = \Delta E_0 + E_0^{expt} - E_0^P$. Here ΔE_0 was the least-squares-refined energy threshold difference, E_0^{expt} was the experimentally chosen energy threshold, and E_0^P was the edge position energy.[33] [b] The coordination numbers are given via the FABM method.

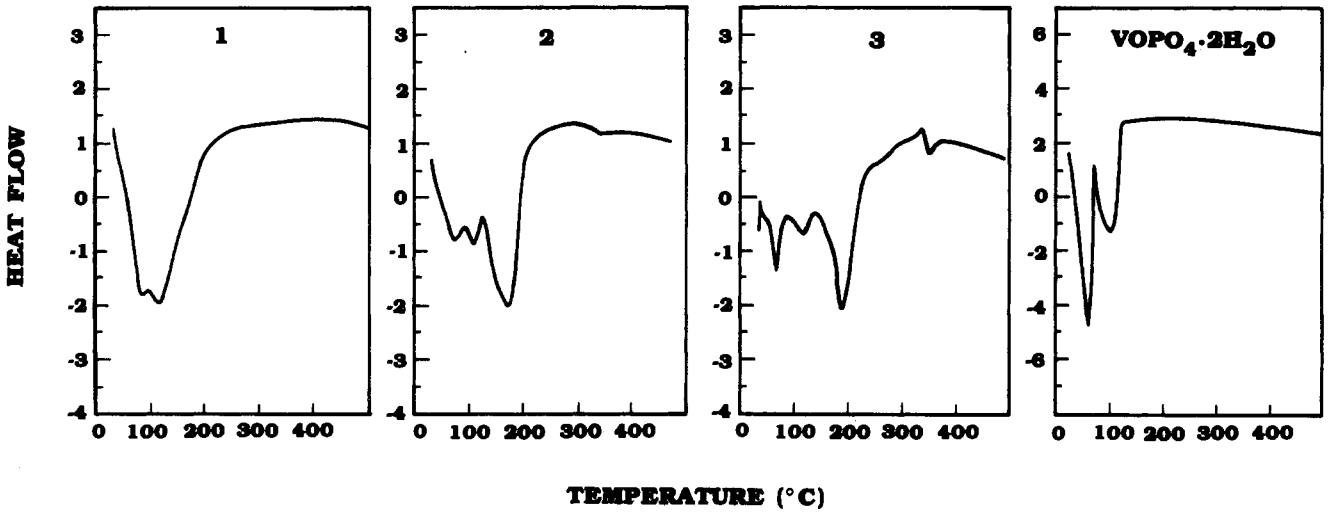

Figure 5. Differential scanning calorimetry (DSC) endotherms for **1**–**3** and the $VOPO_4 \cdot 2H_2O$ parent complex recorded under dinitrogen.

interlayer distance in the parent is 7.40 (2) Å. The Ni intercalate undergoes the least contraction (ca. 0.5 Å) with a [001] interlayer distance of 6.84 (2) Å. This is in line with the EXAFS analysis (vide supra), which indicates that the Ni ions in **3** are six-coordinate and both the Fe and Co ions in **1** and **2** are four-coordinate. The [001] distances for **1** and **2** are virtually equivalent [6.67 (2) and 6.64 (2) Å, respectively] and significantly less than that for **3**.

Thermal Analysis. The DSC endotherms for $VOPO_4 \cdot 2H_2O$ and intercalation compounds **1**–**3** are shown in Figure 5. From the weight loss determined by TGA, it was calculated that the parent compound contains a total of 1.9 water molecules per vanadium; approximately one H_2O molecule was driven off at 70 °C and another at 110 °C. Intercalates **2** and **3** both have 2.3 water molecules per vanadium. They exhibited a weight loss corresponding to about one water molecule at the same temperatures as the parent (i.e., $^1/_2$ molecule at 70°C and $^1/_2$ molecule at 110 °C). Each lost a second water molecule at a higher temperature: 190 °C for **2** and 175 °C for **3** (see Figure 5). It seems possible that this latter water molecule was present as a ligand in the coordination sphere of the intercalating cation. The iron intercalate was found to have a total of 2.8 water molecules. The endotherms accompanying the water loss were not as well resolved as in the other samples, but the DSC data for **1** do show distinct minima at 85 and 120 °C and a very weak shoulder at about 150 °C (Figure 5).

Vibrational Spectra. The decrease in crystallinity upon intercalation is again illustrated, this time by the broadening of the Raman spectral bands for **1**–**3** in comparison with those for the $VOPO_4 \cdot 2H_2O$ parent complex (Figure 6). In the spectrum of the parent, the strong bands near 940 and 1030 cm^{-1} can be assigned to the P–O stretching vibration of the $[PO_4]^{3-}$ group and the V–O stretching vibration of the $[V{=}O]^{3+}$ group,[43,44] respectively. The weaker bands between 500 and 600 cm^{-1} are bending modes. Upon intercalation, the two major bands broaden and shift by ca. 20 cm^{-1} to lower frequencies. The frequency shifts are presumably due to the fact that, upon intercalation, the vanadium is partially reduced from a 5+ oxidation state in $VOPO_4 \cdot 2H_2O$ to a "4.6+" formal charge in **2** and **3**, and a "3.8+" formal charge in **1**. This reduction would be expected to cause a weakening of the $[V{=}O]^{3+}$ bond and could also affect the $[PO_4]^{3-}$ vibration. Thus, it is reasonable that both bands would be shifted to lower frequencies as shown in Figure 6 for **1**–**3**. The bending vibrations are expected to be much less sensitive to the slight changes in the interatomic distances associated with the reduction of vanadium; hence, they would not be expected to exhibit large frequency shifts.

Examination of the O–H stretching (3300–3600 cm^{-1}) and bending (ca. 1620 cm^{-1}) bands in the mid-infrared spectra for **1**–**3** and $VOPO_4 \cdot 2H_2O$ (Figure 7) further supports the DSC results. The sharp bands near 3600 and 1620 cm^{-1} in the spectrum of the parent compound are due to strongly bonded water molecules within the crystalline lattice.[45] These O–H vibrational modes

(43) Bhargava, R. N.; Condrate, R. A., Sr. *Appl. Spectrosc.* **1977**, *31*, 230.
(44) (a) Stranford, G. T.; Condrate, R. A., Sr. *J. Solid State Chem.* **1984**, *52*, 248. (b) Stranford, G. T.; Condrate, R. A., Sr. *Spectrosc. Lett.* **1984**, *17*, 85.
(45) R'kha, C.; Vandenborre, M. T.; Livage, J.; Prost, R.; Huard, E. *J. Solid State Chem.* **1986**, *63*, 202.

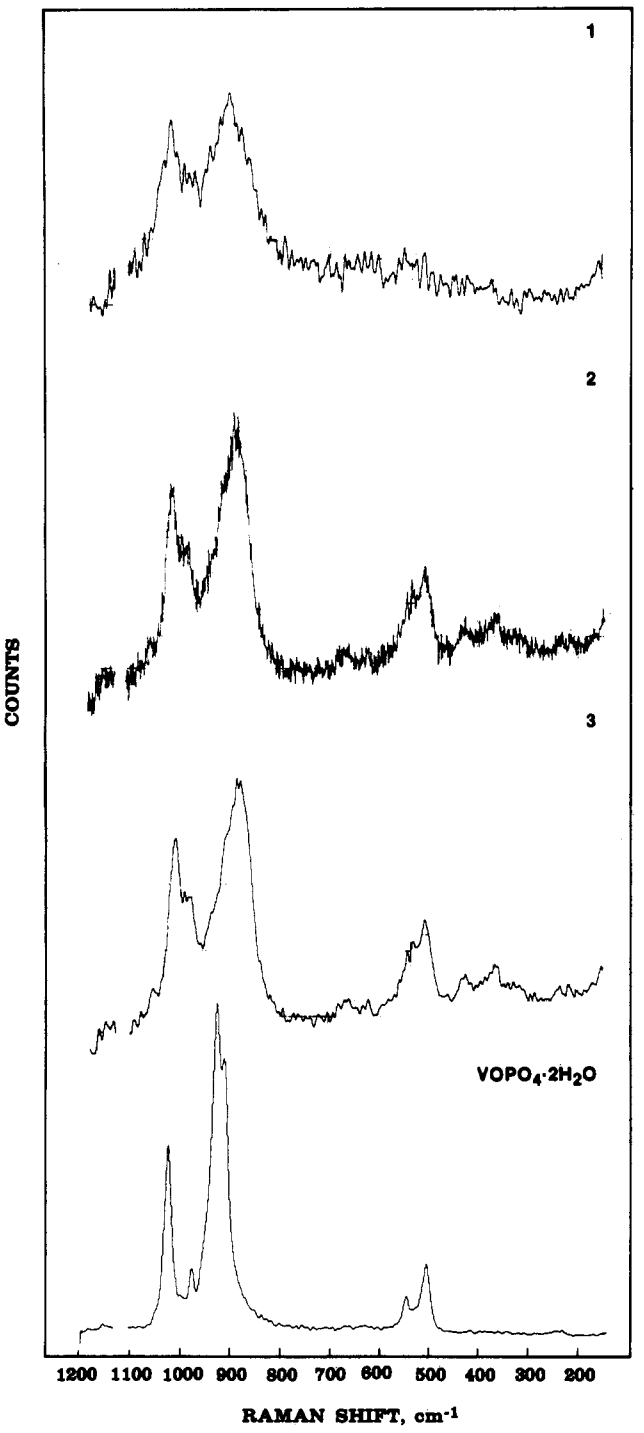

Figure 6. Raman spectra of **1–3** and the $VOPO_4 \cdot 2H_2O$ parent complex (5145-Å excitation).

are probably associated with the water molecule bound to vanadium [V–OH_2; 2.233 (6) Å],[39] which, in turn, may be the water molecule that is driven off at 110 °C by thermal analysis (Figure 5). Additional lattice water, which is apparently less tightly bound in the van der Waals gap, is indicated by the broad bands near 3300 and 1620 cm^{-1} in the spectrum of the parent (Figure 7). Note that for the bending vibration at 1620 cm^{-1}, sharp and broad bands are superimposed. The broad band is likely to be associated with the water molecule located midway between adjacent V–P–O layers at half of the unit cell repeat distance along *c* from the phosphorus atoms [P–OH_2; 3.705 (1) Å].[39] As such, it may be the molecule that is driven off at 70 °C by thermal analysis.

In the O–H stretching and bending regions, the infrared spectrum (Figure 7) for the nickel intercalate (**3**) is nearly identical with that for the $VOPO_4 \cdot 2H_2O$ parent complex. However, for the cobalt intercalate (**2**), the infrared spectrum shows considerable

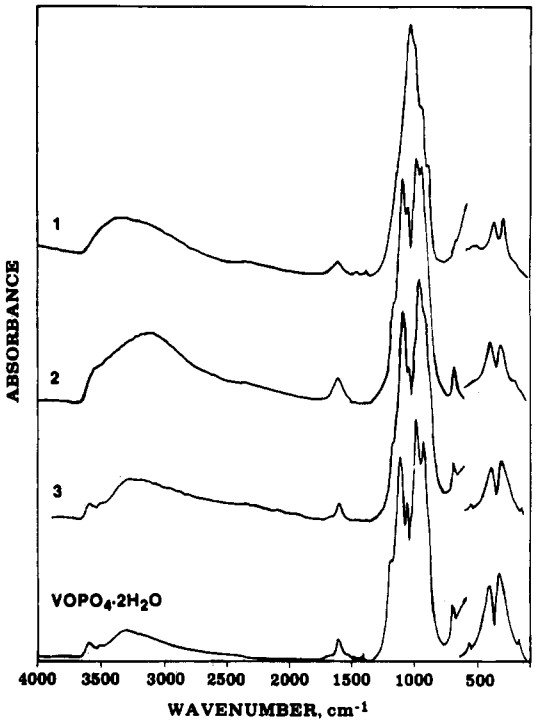

Figure 7. Infrared spectra obtained on Fluorolube mulls in the OH stretching region of **1–3** and the $VOPO_4 \cdot 2H_2O$ parent. Infrared spectra were obtained on KBr pellets (above 500 cm^{-1}) and Nujol mulls (below 500 cm^{-1}).

broadening of the O–H bands; the 3600-cm^{-1} O–H stretching band, due to tightly bound water molecules (i.e., V–OH_2), is seen here (Figure 7) as a shoulder on the large, broad O–H band at ca. 3150 cm^{-1}, which is presumably due to nonbonded water molecules within the van der Waals gap. The O–H regions in the infrared spectrum of the iron intercalate (**1**) are different from those of either **2** or **3**. The spectrum for **1** (Figure 7) does not show any evidence for the presence of strongly bonded water molecules within the V–P–O lattice.

The infrared spectra for **1–3** and $VOPO_4 \cdot 2H_2O$ between 1500 and 100 cm^{-1} are also shown in Figure 7. Johnson and Jacobson have reported[18b] that $V^{5+}{=}O$ and $V^{4+}{=}O$ absorb at 1013 and 992 cm^{-1}, respectively, in $VOAsO_4 \cdot 2H_2O$ intercalation compounds. For $VOPO_4 \cdot 2H_2O$ intercalation compounds, however, this region (between 900 and 1200 cm^{-1}) is very difficult to interpret due, in part, to the fact that phosphates and V–O moieties absorb at nearly the same frequencies. The infrared data are further complicated by the mixing of P–O and V–O modes.[44,45] The spectra of **2** and **3** are quite similar to the spectrum of the parent compound. Only slight band ratio changes are evident, thus suggesting that there are only minor perturbations of the parent structure upon intercalation with Co and Ni. The medium band at 680 cm^{-1} observed in the spectrum of the parent is due to the V–O–P bending vibration;[43] it is also observed and unshifted in the spectra for **1–3** (see Figure 7). Bands below 500 cm^{-1} are probably lattice modes and show only small changes upon intercalation. In the 900–1200-cm^{-1} region, the spectrum of **1** appears to be very different from the spectra of **2**, **3**, and pristine $VOPO_4 \cdot 2H_2O$. The presence of an additional water molecule in **1** and the mixing of modes might induce the observed differences. The more amorphous nature of **1** also compounds the difficulty of interpreting its infrared spectrum.

Site Occupancy. With the information presented above, we can postulate how the intercalants may fit into the parent structure. The local symmetry around the divalent nickel ions in **3** is likely to be octahedral with an approximate O–Ni–O distance of 6.9 Å (Ni–O bond length 2.05 Å and a van der Waals radius of 1.4 Å for oxygen). Octahedral structures have a 4-fold symmetry as do the proposed intercalation sites (vide supra), and the dimensions of these intralayer pockets (ca. 6.2 × 6.2 Å) are sufficient

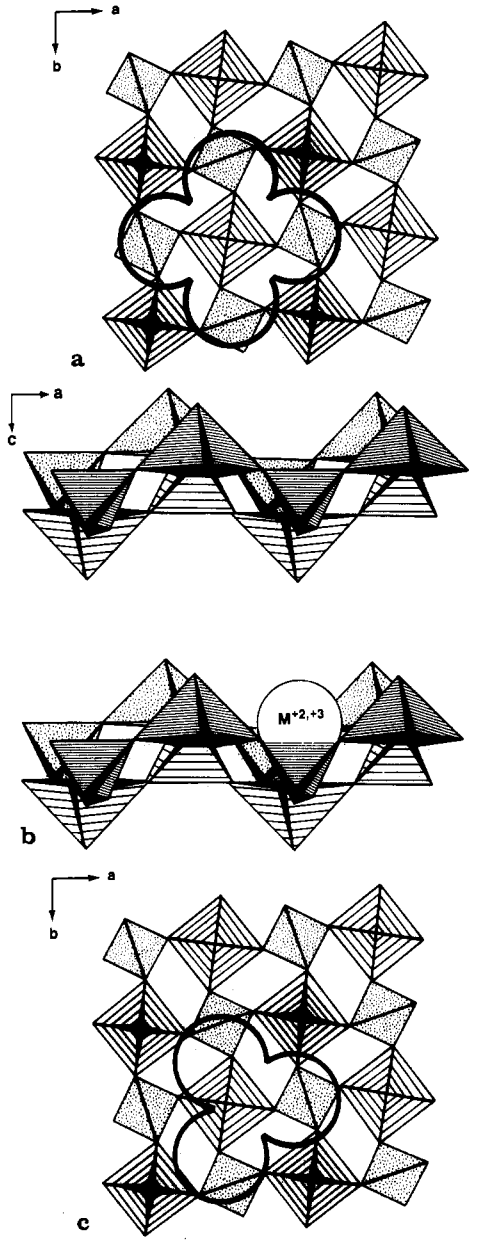

Figure 8. (a) Schematic illustration of the proposed site occupancy of a NiO_6 octahedron within the $VOPO_4{\cdot}2H_2O$ parent lattice, as viewed down the *c* axis. The thick line in the shape of a four-leaf clover represents the perimeter of the four equatorial Ni–O interactions. (b) A schematic view down the *b* axis of the structure of $VOPO_4{\cdot}2H_2O$ showing the proposed location of an intercalating metal (M) cation (Ni^{2+}, Co^{2+}, Fe^{3+}). (c) Schematic illustration of the proposed site occupancy of a CoO_4 tetrahedron within the parent lattice, as viewed down the *c* axis. The thick line in the shape of a clover leaf represents the perimeter of three Co–O interactions.

to accommodate the NiO_6 groups. Figure 8a shows a schematic illustration of the proposed site occupancy of a NiO_6 octahedron within the host lattice as projected onto the *ab* plane. Figure 8b shows a complimentary view of the intercalating, divalent nickel cation within the host lattice as projected onto the *ac* plane. If there are water molecules coordinated to the Ni^{2+} ions, then multiple hydrogen bonding with the oxygen atoms of four in-plane vanadyl groups (see Figure 8a) would be expected to hold the Ni ions in the intralayer V–P–O cavities. This particular site occupancy defines a second shell of eight oxygen atoms (at the corners of four in-plane PO_4 and VO_6 polyhedra) around the first shell of six oxygen atoms about nickel in **3**. These distant, nonbonded oxygen atoms might account for the strong second-shell backscattering seen in the Fourier transform of the Ni EXAFS data for **3** (Figure 2c). In order to test this hypothesis, the Fourier-filtered EXAFS, $k^3\chi(k)$ vs. k, for the distant coordination sphere (filtering window 1.9–3.3 Å) were subjected to the curve-fitting procedure (vide supra) using oxygen phase and amplitude functions. A good fit to these data was obtained (see supplementary material). The resulting FABM structural parameters indicate that the second-shell Ni–O coordination sphere for **3** is composed of 7.6 ± 1 oxygen atoms (σ = 0.097 (25) Å) at 3.02 (4) Å (ΔE_0^P = 12.54 eV).

For **2**, the Co^{2+} ions exhibit 4-fold coordination with an average Co-O bond length of 2.03 (1) Å. Tetrahedral coordination about Co^{2+} ions is quite common, and hence, it reasonably follows that the local symmetry around cobalt in **2** is likely to be just that. Unlike the proposed intralayer sites that have 4-fold symmetry, tetrahedral CoO_4 groups possess a 3-fold symmetry. Hence, although the divalent Co ions in **2** can clearly be accommodated within the V–P–O pockets (see Figure 8b), extensive hydrogen bonding by water molecules, which are presumably coordinated to cobalt, with the host lattice vanadyl groups (as suggested above for the octahedral Ni^{2+} coordination environment in **3**) is now not tenable due to the symmetry mismatch. Figure 8c shows a schematic illustration of the proposed site occupancy of a CoO_4 tetrahedron within the host lattice as projected onto the *ab* plane. The fact that the Fourier transform of the Co EXAFS data for **2** (Figure 2b) does not conclusively exhibit a second-shell peak suggests that the Co ions may indeed be more mobile both within a given pocket and, possibly, among adjacent ones.

As postulated for the Co^{2+} ions in **2**, the local symmetry around the Fe^{3+} ions in **1** is also likely to be tetrahedral, albeit high-spin Fe^{3+} tetrahedral complexes are much less common than tetrahedral Co^{2+} ones. Unlike the cobalt and nickel intercalates, which have a transition-metal ion intercalant loading level of ca. 20% (relative to 100% V), the iron intercalate has about twice the interlayer intercalant ion loading. A possible explanation for the higher loading is that since iron has the smallest ionic radius and the highest formal charge (cf. Fe^{3+}, Co^{2+}, Ni^{2+}) of the intercalants studied, it may pack more densely among the van der Waals sites due to simple steric effects. However, with the dramatic decrease in the long-range intra- and interlayer order for **1** (as is evident from the powder XRD results, vide supra) and the lack of supporting EXAFS evidence for a distant coordination sphere about Fe, the ferric ions might be fluxional in the interlayer environment. In considering this possibility, it must be remembered that the iron intercalate has a third water of hydration for which to account. The infrared spectra show that the short-range intralayer structure in **1** is more perturbed than that for either **2** or **3**, but there is no evidence indicating a complete disruption of the parent $VOPO_4{\cdot}2H_2O$ structure.

Conclusions

For intercalates **1**–**3**, chemical and physical analyses indicate that the vanadium(5+) in the pristine parent complex ($VOPO_4{\cdot}2H_2O$) is reduced upon intercalation by iron, cobalt, and nickel. XRD and Raman measurements indicate that the long-range intra- and interlayer order (i.e., crystallinity) of the parent lattice decreases upon intercalation. IR data show that the short-range interatomic host structure (e.g., V–O, P–O) remains essentially intact for **1**–**3**. The local environments of the iron, cobalt, and nickel intercalants are known; bond distances, Debye–Waller factors, and coordination numbers were established by EXAFS. The data suggest that Fe^{3+} and Co^{2+} ions in **1** and **2** are four-coordinate (presumably tetrahedral) with oxygen neighbors at 1.95 (2) and 2.03 (1) Å, respectively. The Ni^{2+} ions in **3** are six-coordinate (presumably octahedral) with a first shell of oxygen neighbors at 2.05 (2) Å and a second, distant shell of approximately 8 ± 1 oxygen atoms at 3.02 (4) Å. An intercalation site, defined by four in-plane VO_6 groups, was proposed for the divalent Co and Ni ion occupancies within the van der Waals gap. It was further proposed that the symmetry of the six-coordinate (aquo) environment around Ni in **3** facilitates considerable hydrogen bonding with the parent V–P–O lattice, thereby fixing the Ni^{2+} intercalant in interlayer pockets. The iron intercalate (**1**) is significantly different from the other systems; the iron atoms in

1 are trivalent rather than divalent (as in 2 and 3), and there is about twice the transition-metal ion load for 1 than for either 2 or 3. Also, 1 has an additional water of hydration and perturbs the host structure to a greater degree than either 2 or 3.

Acknowledgment. We thank Dr. Susan M. Kauzlarich (Michigan State University/University of Virginia) for her assistance with the X-ray absorption measurements, and we wish to acknowledge our Standard Oil Co. colleagues Mary Ann Hazle, Drs. Sampath S. Iyengar and Raymond G. Teller, and Martin L. Mittleman for their technical assistance and helpful discussions.

Supplementary Material Available: Details of the FABM method, including references and a table of FABM regression coefficients, and Figures I–III (the primary X-ray absorption data in the form ln (I_0/I) vs. E (in eV) and the background-subtracted and Fourier-filtered data, $k^3\chi(k)$ vs. k for 1–3), Figures IV–VII (FABM correlation curves ΔE_0^P vs. Δr, B vs. σ, Σ^2 vs. Δr, and Σ^2 vs. σ), and Figure VIII (Fourier-filtered $k^3\chi(k)$ vs. k data for the second-shell Ni–O interaction in 3 and the best fit to these data) (26 pages). Ordering information is given on any current masthead page.

Contribution from the Departments of Chemistry, University of Florence, I-50144 Firenze, Italy, Facultad de Ciencias Quimicas, University of Valencia, Valencia, Spain, and University of Siena, Siena, Italy

Synthesis and Complexing Properties of the Large Polyazacycloalkane 1,4,7,10,13,16,19,22,25,28-Decaazacyclotriacontane (L). Crystal Structure of the Monoprotonated Dicopper(II) Complex $[Cu_2(L)HCl_2](ClO_4)_3 \cdot 4H_2O$

Andrea Bencini,[1a] Antonio Bianchi,[1a] Enrique Garcia-España,[1b] Mauro Giusti,[1a] Stefano Mangani,[1c] Mauro Micheloni,*[1a] Pierluigi Orioli,[1a] and Piero Paoletti*[1a]

Received September 4, 1986

The synthesis and characterization of the large aza macrocycle 1,4,7,10,13,16,19,22,25,28-decaazacyclotriacontane (L) ([30]aneN$_{10}$) are described. Crystals of the compound $[Cu_2(L)HCl_2](ClO_4)_3 \cdot 4H_2O$ are monoclinic, space group $P2/n$, with a = 21.491 (5) Å, b = 7.696 (4) Å, c = 12.210 (4) Å, β = 103.04 (5)°, and Z = 2. Refinement of the atomic parameters by least-squares methods gave a final R factor of 0.097 (R_w = 0.097) for 1298 unique reflections with $I > 3\sigma(I)$. The structure consists of binuclear $[Cu_2(L)HCl_2]^{3+}$ cations and perchlorate anions; each half of the macrocycle is symmetry related by a twofold axis passing through its center. The copper atoms (Cu–Cu distance 7.26 (1) Å) are coordinated by four nitrogen atoms of the macrocycle ligand (average Cu–N = 2.03 (2) Å) and one chloride ion (Cu–Cl = 2.43 (1) Å) in a square-pyramidal geometry. One of the two uncoordinated nitrogen atoms is protonated. The basicity constants of the macrocycle and the stability constants of the copper(II) complexes were determined by potentiometry at 25 °C in 0.15 mol dm^{-3} $NaClO_4$. The formation enthalpy of the species $[Cu_2(L)]^{4+}$ was determined by batch microcalorimetry. Only binuclear species are formed; the stability of the binuclear $[Cu_2(L)]^{4+}$ species is high (log K = 37.77), and its formation is largely exothermic ($\Delta H°$ = −45.5 kcal mol^{-1}). The thermodynamic quantities $\Delta G°$ and $\Delta H°$ as well as the electronic spectral features of the $[Cu_2(L)]^{4+}$ species indicate that all nitrogen atoms are coordinated to the copper(II) atoms. The $[Cu_2(L)]^{4+}$ macrocycle shows a great tendency to form protonated and hydroxo species: $[Cu_2(L)H]^{5+}$, $[Cu_2(L)H_2]^{6+}$, $[Cu_2(L)H_3]^{7+}$, and $[Cu_2(L)OH]^{3+}$ are the species present at equilibrium.

Introduction

Little investigative work has been done with large aza macrocycles.[2-4] The preferred binucleating tendency (rather than mononucleating) of these ligands, together with the possible suitability for "anion coordination" studies[5] and "supercomplex" formation,[6] provides confirmation that these macrocyclic ligands display some interesting complexation chemistry. The adjective "large" has been used to describe polyazacycloalkanes having more than six nitrogen donor atoms.[3] The largest polyazacycloalkane so far investigated contained nine nitrogen donor atoms and two copper(II) ions.[7] In recent papers, studies on the three large polyazacycloalkanes 1,4,7,10,13,16,19-heptaazacycloheneicosane ([21]aneN$_7$),[4] 1,4,7,10,13,16,19,22-octaazacyclotetracosane ([24]aneN$_8$),[3] and 1,4,7,10,13,16,19,22,25-nonaazacycloheptacosane ([27]aneN$_9$)[7] have been reported. We have now synthesized and characterized the large polyazacycloalkane 1,4,7,10,13,16,19,22,25,28-decaazacyclotriacontane ([30]aneN$_{10}$) (abbreviated as (L)) and studied its ligational behavior toward hydrogen (basicity) and copper(II) ions.

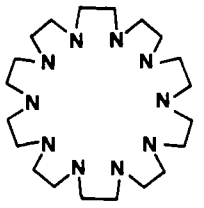

L

Experimental Section

Ligand Synthesis. The overall synthetic path followed to obtain the macrocyclic ligand is reported in Figure 1. All chemicals were reagent grade and were utilized without further purification.

1,4,7,10,13-Pentakis(*p*-tolylsulfonyl)-1,4,7,10,13-pentaazatridecane (b). The starting material was obtained from the commercial 1,4,7,10,13-pentaazatridecane (a) (Fluka product) by double distillation under reduced pressure. The fraction collected was that between 265 and 270 °C at 0.1 Torr. A solution of a (19.9 g, 0.105 mol) in 100 cm^3 of pyridine was added to a solution of *p*-toluenesulfonyl chloride (100 g, 0.53 mol) in 300 cm^3 of pyridine placed in a 1 dm^3 four-necked round-bottom flask equipped with a mechanical stirrer. The addition of the pentaamine (a) solution was carried out in such a way that the reaction temperature was kept at 40–50 °C. After the addition, the reaction mixture was maintained at 50 °C for 2 h and then was allowed to cool at room temperature and added to a vigorously stirred mixture of water and ice (2.5 dm^3) containing the amount of concentrated HCl necessary to

(1) (a) University of Florence. (b) University of Valencia. (c) University of Siena.
(2) Atkins, T. J.; Richman, J. E.; Dettle, W. F. *Org. Synth.* **1978**, *58*, 86.
(3) Bianchi, A.; Mangani, S.; Micheloni, M.; Nanini, V.; Orioli, P.; Paoletti, P.; Seghi, B. *Inorg. Chem.* **1985**, *24*, 1182.
(4) Micheloni, M.; Paoletti, P.; Bianchi, A. *Inorg. Chem.* **1985**, *24*, 3702.
(5) Graf, E.; Lehn, J. M. *J. Am. Chem. Soc.* **1976**, *98*, 6403. Dietrich, B.; Hosseini, M. W.; Lehn, J. M.; Session, R. B. *J. Am. Chem. Soc.* **1981**, *103*, 1282. Kimura, E.; Sakonaka, A.; Yatsunami, T.; Kodama, M. *J. Am. Chem. Soc.* **1981**, *103*, 3041.
(6) Peter, F.; Gross, M.; Hosseini, M. W.; Lehn, J. M. *J. Electroanal. Chem. Interfacial Electrochem.* **1983**, *144*, 279. Manfrin, M. F.; Sabbatini, N.; Moggi, L.; Balzani, V.; Hosseini, M. W.; Lehn, J. M. *J. Chem. Soc., Chem. Commun.* **1984**, 555. Garcia-España, E.; Micheloni, M.; Paoletti, P.; Bianchi, A. *Inorg. Chim. Acta* **1985**, *102*, 9.
(7) Bencini, A.; Bianchi, A.; Garcia-España, E.; Giusti, M.; Micheloni, M.; Paoletti, P. *Inorg. Chem.* **1987**, *26*, 681.

0020-1669/87/1326-1243$01.50/0